Steady-State Modeling and Experimental Measurement of a Baffled Impeller Stirred Tank

Albert D. Harvey III and Cassian K. Lee
The Dow Chemical Company, Plaquemine, LA 70765

Stuart E. Rogers
NASA Ames Research Center, Moffett Field, CA 94035

An approximate steady-state method is devised for computing the flow field in a baffled, impeller-stirred tank reactor. The flow field in a cylindrical tank with a 45° pitched-blade impeller rotating at 100 rpm and four stationary rectangular side-wall baffles is simulated using a new approximate steady-state approach. The method provides an alternative to a full unsteady Navier–Stokes simulation. The new steady-state analysis involves accurately defining the geometry of the mixing tank using a multiblock grid technique. The flow is solved from a rotating frame of reference for a single position of the impeller relative to the side-wall baffles. The steady-state numerical results are then spatially averaged and compared with time-averaged data obtained experimentally using laser Doppler velocimetry (LDV). Spatially averaged numerical predictions obtained using this approximate steady-state method for the radial and axial velocity components agree well with the LDV data. The predicted magnitude of the tangential velocity component, however, is higher than the experimentally measured values. Closer agreement of the tangential velocities with experimental values is obtained using a finer grid and it is found that a relatively fine grid is needed for accurately predicting the tangential velocity magnitude. Use of this approximate steady-state method allows designers of mixing vessels to obtain flow-field results for baffled vessels much more efficiently than using full unsteady Navier–Stokes simulations.

Introduction

Impeller-stirred reactors are widely used in the chemical industry as a vessel whereby chemical reactants can be efficiently mixed to initiate reaction for the creation of the desired products. Knowledge of factors such as residence time, concentration levels, and mixing efficiency are critical to the successful operation of the impeller-stirred reactor. Initially, industrial applications of these vessels are typically applied at a small pilot- or bench-scale unit that facilitates controlled conditions for the careful measurement and study of these key operating factors. After the process has been proved at this test scale the process is then typically scaled up to an appropriate commercial size production unit. Usually the commercial scale operating conditions are such that accurate measurement techniques become difficult and often impossible. Also, this scale-up is sufficiently complex so as to warrant a procedure whereby scale-up takes place in several successive stages, each stage becoming larger than its successor, incurring not only the cost of the final process, but also the cost of each intermediate process.

Computational techniques can significantly reduce the cost associated with this scale-up process by verifying the performance of large-scale units before their actual manufacture, and provide an aid in making critical reactor design decisions. Before any computational results can be deemed reliable enough to influence design decisions, the computational model must be validated using experimental data. The present work is part of a research effort aimed at developing and validating a set of computational tools to numerically study the flow field inside an impeller-stirred mixing tank. These computational tools include a multiblock grid-generation program, and an incompressible Navier–Stokes code.

Correspondence concerning this article should be addressed to A. D. Harvey.
Present address for C. K. Lee: Midland, MI 48674.

The grid-generation program is capable of representing the geometry of a variety of impeller and side-wall baffle designs contained inside a cylindrical vessel using multiple zones that are patched together.

There are numerous works on unbaffled mixing tank computations in three dimensions using a rotating coordinate system. Hiraoka et al. (1988) studied the flow surrounding one blade of a paddle-type impeller using this technique. They found that the fluid moved inward toward the impeller shaft far away from the impeller and radially outward toward the tank wall near the impeller. In this work, numerical results were compared to experimental laser Doppler velocimetry (LDV) data; the primary difference between the two occurred near the impeller shaft. Kaminoyama and Kamiwano (1991) studied the flow in a tank stirred by a paddle-type impeller by choosing the domain as the region between two blades of the impeller. In this work the time dependence of the flow was also examined. For the given system, a steady-state condition was reached in about 5 s.

For the case of baffled tanks, the effect of the rotating impeller blades passing the stationary side-wall baffles prohibits a strict application of the rotating coordinate system approach. The flow inside the baffled tank is, in general, time-dependent, regardless of the reference frame chosen. A modified version of the INS3D finite difference code developed by Rogers et al. (1992) and Rogers and Kwak (1990, 1991, 1987) is used in the present work. For performing full unsteady computations of baffled impeller-stirred tanks, a rotating grid scheme has been incorporated into the INS3D code to simulate the relative motion between a rotating impeller and stationary baffles. This time-dependent approach uses a combination of rotating and stationary grid zones. The interface between the inner rotating zones and the outer stationary zones are treated using a dynamic (time-dependent) patching technique that avoids interpolation of flow-field quantities. This moving grid algorithm is the subject of future work and, due to the unsteady three-dimensional nature of the flow, is somewhat compute intensive. Current work on unsteady grid techniques applied to the impeller-stirred reactor has been published by Gosman et al. (1992), and Preng and Murthy (1992).

In the present work, some approximate steady-state techniques of modeling the flow in a baffled impeller-stirred tank are discussed. One of these steady-state techniques is then used to study the flow induced by a rotating 45° pitched-blade impeller in a tank with stationary, rectangular side-wall baffles. Although these steady-state methods are less rigorous than full unsteady, three-dimensional Navier–Stokes simulations, they can be performed with fewer resources, which allows the designer of mixing equipment to investigate a broader range of designs in less time.

One of these steady-state approximate approaches is to neglect the side-wall baffles altogether. The problem can then be solved using the rotating frame of reference attached to the impeller as in the works described earlier. The resulting computed velocity field very close to the impeller can then be time-averaged, and this time-averaged profile can be used as a boundary condition for a more detailed steady-state simulation with the baffles replaced in the tank. This two-step method of simulating the unsteady flow in a baffled mixing tank can be performed much more quickly than a full unsteady simulation. The result, however, is a time-averaged flow field instead of the periodic unsteady velocity field that would have resulted from the full unsteady simulation.

Another steady-state approach to the baffled tank problem, which is the subject of the present investigation, is to neglect the relative motion between the impeller and the baffles and solve the problem from a frame of reference attached to the rotating impeller. That is, the problem is solved numerically for a single position of the impeller relative to the side-wall baffles. The results are then spatially averaged to obtain an approximate time-averaged velocity field, which is, quite often, sufficient for engineering purposes. It is shown in subsequent sections that the spatially averaged velocity field obtained from this steady simulation approach, neglecting the relative motion between the impeller and side-wall baffles, is in very good agreement with the time-averaged velocity field measured experimentally. For higher Reynolds numbers, it is expected that the side-wall baffles would have a greater effect on the flow and an unsteady approach must be considered.

To compute the flow in a rotating frame of reference, additional force terms are employed similar to the method of Kiris et al. (1993). The following section outlines the resulting governing equations and method of solution. In subsequent sections, computed results for the flow field induced by a rotating pitched-blade impeller are presented and compared with experiment.

Governing Equations

The incompressible Navier–Stokes equations with the additional inclusion of the time derivative of pressure on the continuity equation introduced by the pseudocompressibility method can be written as follows:

$$\frac{\partial \boldsymbol{Q}}{\partial \tau}+\frac{\partial}{\partial \xi}(\boldsymbol{E}-\boldsymbol{E}_v)+\frac{\partial}{\partial \eta}(\boldsymbol{F}-\boldsymbol{F}_v)+\frac{\partial}{\partial \zeta}(\boldsymbol{G}-\boldsymbol{G}_v)+\boldsymbol{S}_{\text{cen}}+\boldsymbol{S}_{\text{cor}}=0, \quad (1)$$

where the inviscid fluxes in the transformed curvilinear coordinate system are written as

$$\boldsymbol{Q}=\frac{1}{J}\begin{bmatrix} p \\ u \\ v \\ w \end{bmatrix}, \qquad \boldsymbol{H}=\frac{1}{J}\begin{bmatrix} \beta U \\ u(\kappa_t+U)+\kappa_x p \\ v(\kappa_t+U)+\kappa_y p \\ w(\kappa_t+U)+\kappa_z p \end{bmatrix}$$

$$\boldsymbol{S}_{\text{cen}}=\frac{1}{J}\begin{bmatrix} 0 & 0 & 0 & 0 \\ 0 & -(\omega_y^2+\omega_z^2) & \omega_x\omega_y & \omega_x\omega_z \\ 0 & \omega_x\omega_y & -(\omega_x^2+\omega_z^2) & \omega_y\omega_z \\ 0 & \omega_x\omega_z & \omega_y\omega_z & -(\omega_x^2+\omega_y^2) \end{bmatrix}\begin{bmatrix} 0 \\ x \\ y \\ z \end{bmatrix}$$

$$\boldsymbol{S}_{\text{cor}}=\frac{2}{J}\begin{bmatrix} 0 & 0 & 0 & 0 \\ 0 & 0 & -\omega_z & \omega_y \\ 0 & -\omega_z & 0 & -\omega_x \\ 0 & -\omega_y & \omega_x & 0 \end{bmatrix}\begin{bmatrix} p \\ u \\ v \\ w \end{bmatrix}.$$

Table 1. Block Sizes for Coarse Grid

Zone	Size ($j \times k \times l$)	No. of Points	Total
1	18×25×16	7,200	7,200
2	25×30×20	15,000	22,200
3	25×30×18	13,500	35,700
4	14×30×48	20,160	55,860
5	13×30×48	18,720	74,580
6	12×25×48	14,400	88,980

The contravariant velocities are given by

$$U = \kappa_x u + \kappa_y v + \kappa_z w.$$

In the preceding expressions, the generic inviscid flux, $\boldsymbol{H} = \boldsymbol{E}$, $\boldsymbol{F}$, and $\boldsymbol{G}$, when the generic metric terms, $\kappa = \xi$, η, and ζ, respectively and J is the Jacobian of the generalized coordinate transformation. Due to spatial limitations, the reader is referred to Hoffmann (1989) and Anderson et al. (1984) for details of transforming conservation laws using a standard curvilinear coordinate transformation.

The three viscous flux vectors, $\boldsymbol{E}_v$, $\boldsymbol{F}_v$, and $\boldsymbol{G}_v$, are written as a single generic flux vector $\boldsymbol{H}_v$, using a conventional cyclic index notation in the following manner:

$$\boldsymbol{H}_v = \frac{1}{J}\left(\frac{1}{Re_t}\right)\begin{bmatrix} 0 \\ (\nabla\xi_i\cdot\nabla\xi_i)\dfrac{\partial u}{\partial \xi_i} + (\nabla\xi_i\cdot\nabla\xi_j)\dfrac{\partial u}{\partial \xi_j} + (\nabla\xi_i\cdot\nabla\xi_k)\dfrac{\partial u}{\partial \xi_k} \\ (\nabla\xi_i\cdot\nabla\xi_i)\dfrac{\partial v}{\partial \xi_i} + (\nabla\xi_i\cdot\nabla\xi_j)\dfrac{\partial v}{\partial \xi_j} + (\nabla\xi_i\cdot\nabla\xi_k)\dfrac{\partial v}{\partial \xi_k} \\ (\nabla\xi_i\cdot\nabla\xi_i)\dfrac{\partial w}{\partial \xi_i} + (\nabla\xi_i\cdot\nabla\xi_j)\dfrac{\partial w}{\partial \xi_j} + (\nabla\xi_i\cdot\nabla\xi_k)\dfrac{\partial w}{\partial \xi_k} \end{bmatrix},$$

where $\boldsymbol{E}_v$, $\boldsymbol{F}_v$, and $\boldsymbol{G}_v$ are obtained when $i = 1, 2, 3$, respectively. The source terms $\boldsymbol{S}_{cen}$ and $\boldsymbol{S}_{cor}$ are the centrifugal and Coriolis forces, respectively, and are included when the frame of reference chosen is fixed to the impeller and rotating at a rotational speed of $\Omega = \sqrt{\omega_x^2 + \omega_y^2 + \omega_z^2}$. For the present work rotation takes place strictly around the z-axis, hence ω_x and ω_y are zero.

The preceding equations are nondimensionalized with respect to a reference length $\tilde{x}_{ref}$ and a reference velocity $\tilde{u}_{ref}$ in the standard fashion. Thus, the components of the rotational velocity $\tilde{\omega}_{x_i}$ are nondimensionalized in the following manner:

$$\omega_{x_i} = \frac{\tilde{\omega}_{x_i}}{\tilde{u}_{ref}/\tilde{x}_{ref}}.$$

Table 2. Block Sizes for Medium Grid

Zone	Size ($j \times k \times l$)	No. of Points	Total
1	26×27×32	22,454	22,464
2	36×34×25	30,600	53,064
3	36×34×25	30,600	83,664
4	23×34×76	59,432	143,096
5	19×34×76	49,096	192,192
6	15×27×76	30,780	222,972

Table 3. Block Sizes for Fine Grid

Zone	Size ($j \times k \times l$)	No. of Points	Total
1	60×27×44	71,280	71,280
2	97×34×40	131,920	203,200
3	97×34×45	148,410	351,610
4	29×34×123	121,278	472,888
5	24×34×123	100,368	573,256
6	14×27×123	46,494	619,750

Note that if the rotation is about the z-axis and the reference length, $\tilde{x}_{ref}$, is chosen as the impeller radius, $\tilde{r}_b$, and the reference velocity, $\tilde{u}_{ref}$, is chosen as the impeller tip speed, $\tilde{\omega}_z \tilde{r}_b$, then $\omega_x = 0$, $\omega_y = 0$, $\omega_z = 1$ and the Reynolds number be-

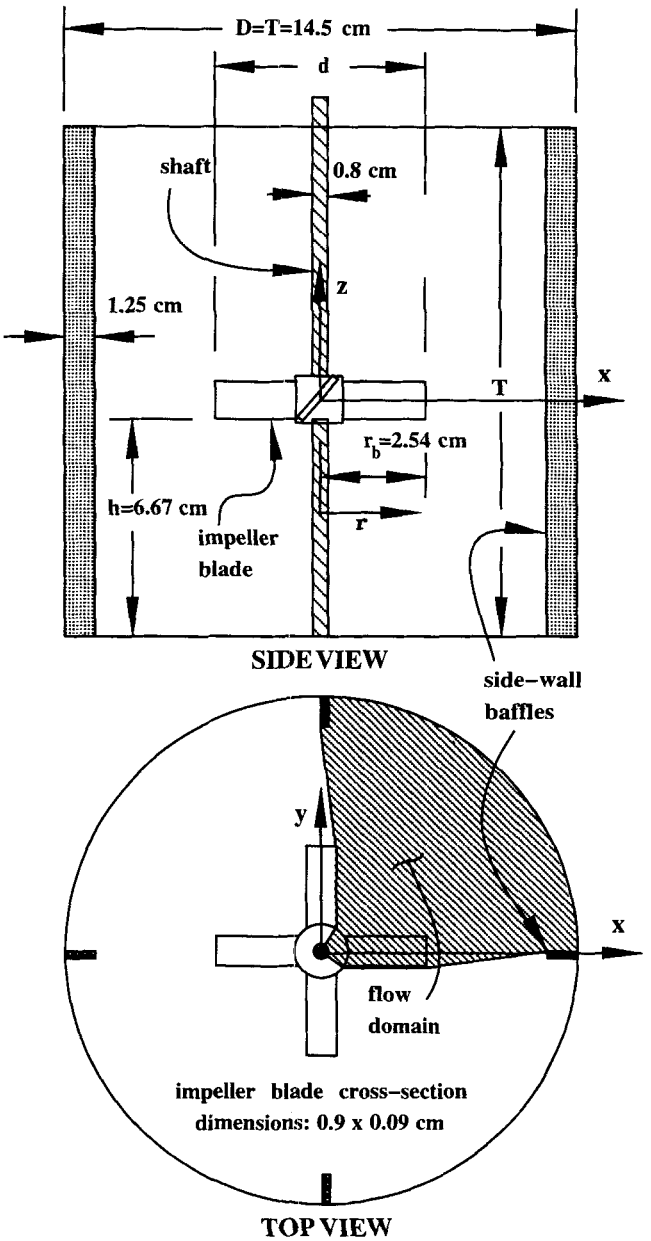

Figure 1. Mixing tank geometry with pitched-blade impeller and four rectangular baffles.

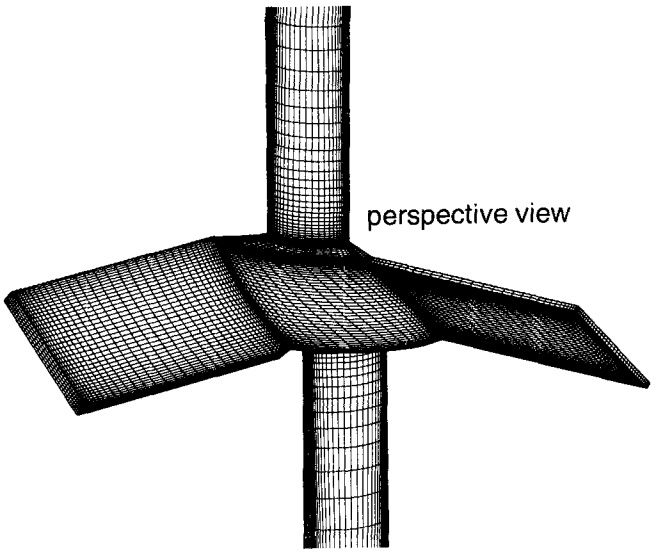

Figure 2. Surface grid for pitched-blade impeller (medium grid).

comes $\mathrm{Re}_t = \tilde{u}_{\mathrm{ref}}\tilde{x}_{\mathrm{ref}}/\tilde{\nu} = \tilde{\omega}_z\tilde{r}_b^2/\tilde{\nu}$. For the case of rotation about the z-axis, the velocity components in the rotating frame of reference (u_r, v_r, w_r) are transformed to the fixed frame of reference (u_a, v_a, w_a) using the following transformation:

$$u_a = u_r + y\omega_z$$
$$v_a = v_r - x\omega_z$$
$$w_a = w_r.$$

Equations 1 are hyperbolic and can be marched in the τ-direction until the residuals are reduced to an acceptable level. Third-order flux-difference splitting (Rogers et al., 1990) is used for the convective terms of Eqs. 1, and second-order central differencing is used for the viscous terms. At each subiteration level, the algebraic system of equations that approximates Eq. 1 is solved using a multidirectional line-relaxation technique. Further details of the numerical algorithm can be found in Rogers et al. (1991).

Computational Gridding

In this section, the geometry is defined using a multiblock grid-generation technique. The multizone body-fitted computational grid consists of six zones. To show grid consistency, solutions are obtained using three different grid densities. Tables 1, 2 and 3 list grid zone attributes for the coarse, medium, and fine grids, respectively. In Figure 1, a four-blade, 45° pitched-blade impeller is shown submerged approximately midway inside a cylindrical tank. The extent of the computational domain is illustrated by the shaded region in the top view. Periodic boundary conditions are imposed in the surface of each blade 90° apart.

The impeller shaft is coincident with the z-axis and extends from the surface to the bottom of the tank. The impeller grid surfaces are illustrated in Figure 2. At the periodic grid plane, two additional layers of grid points are used to update the periodic boundary from the opposite side of the grid in the circumferential direction. Due to the pitch of the impeller blades, the periodic boundaries of the domain are not planar. However, each point on a periodic surface is exactly 90° away from the corresponding point in the other periodic surface. This explains why the shaft above and below the impeller appears shifted slightly in Figure 2. The extent of periodicity is offset slightly by a distance equal to the sweep of the impeller blades.

Six grid zones are used; each of these zones overlaps neighboring zones by two grid cells. In Figure 3, the zonal structure of the computational grid is illustrated. The outline of each grid zone is shown. The computational ξ-coordinate runs radially outward in all zones; the η-coordinate runs circumferentially and the ζ-coordinate runs axially. Thus constant ξ-surfaces appear cylindrical in shape (the outer tank wall is the maximum constant ξ-surface in zone 6). The lowest ξ-surfaces of zones 2 and 3 correspond to the shaft surface where no-slip boundary conditions are applied. Constant η-surfaces appear as surfaces of a constant angular location. Figure 4 illustrates a sectional view of the computational grid.

Zone 1 describes the region directly between the two impeller blades. Zone 2 extends from the tank bottom to the

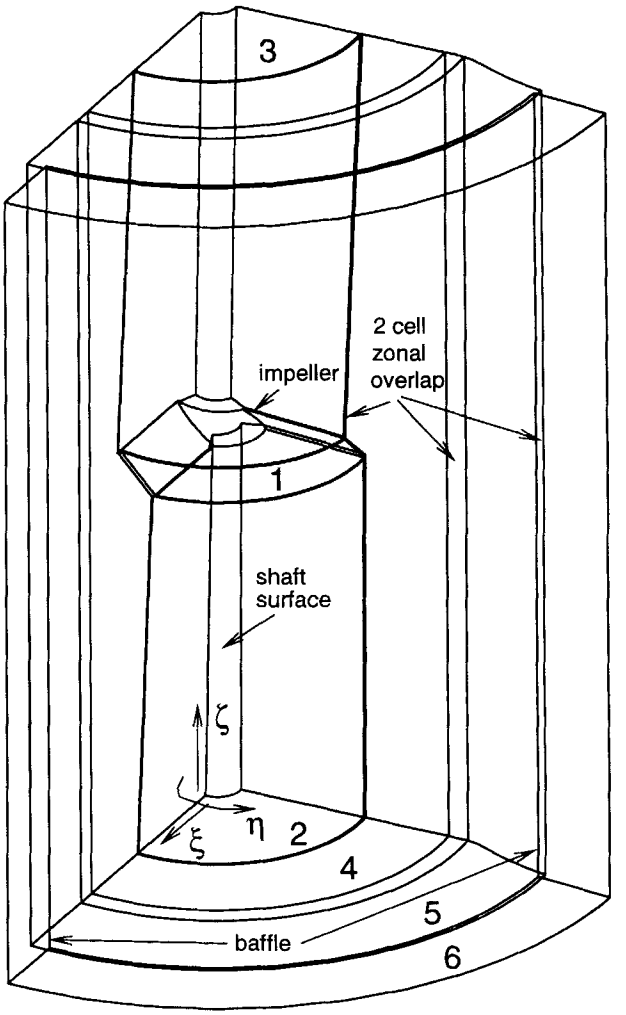

Figure 3. Zonal grid structure showing outline of each grid zone.

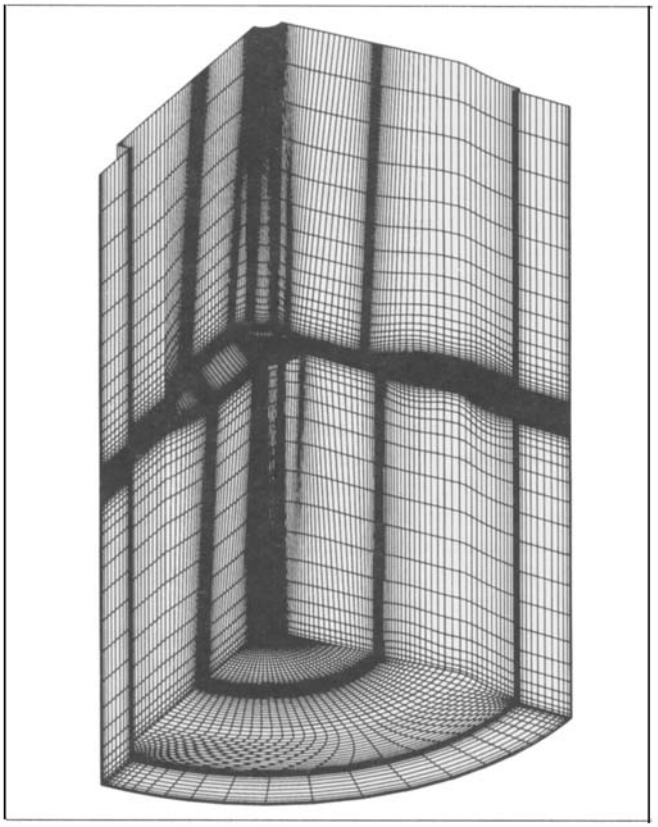

Figure 4. Zonal grid structure showing all solid grid surfaces and periodic grid surfaces (medium grid).

bottom of the impeller. Similarly, zone 3 extends from the top of the impeller to the free surface at the top of the tank. Two additional zones (zones 4 and 5) are wrapped circumferentially around the outside of zones 1, 2 and 3. A sixth zone, which overlaps into zone 5, is used to describe the region between baffles. Zones 1, 2 and 3 overlap by two cells into zone 4. Zone 1 overlaps (in the axial direction) into zone 2 below and zone 3 above. This grid construction is applicable to virtually any mixing tank geometry.

Zone 4 is made to overlap into zone 5 by two cells. The reason for splitting this region between the impeller and baffles into two separate zones is for the purpose of simulating the relative motion between these two components. In a future reporting effort describing an unsteady computational scheme, zones 1–4 will be made to rotate relative to zones 5 and 6 and the interface between zones 4 and 5 changes with time. However, for the present work, all zones are stationary since we are neglecting the relative motion between moving and stationary parts of the flow domain.

The η-boundaries of each zone (excluding zone 1) are updated using a periodic condition. The lowest η-surface is updated using patched zone conditions from the η-surface at $\eta_{max} - 2$. Similarly, the highest η-surface is updated by injection of values from the $\eta = 3$ grid surface. The highest and lowest η-surfaces in zone 1 are no-slip boundaries corresponding to the impeller blade surfaces.

The boundaries of zones that overlap into adjacent zones all match point-for-point with the neighboring zone and direct injection of solution values are imposed. For example, the high value of the ξ-coordinate in zone 4 is updated by direct injection of values at $\xi = 3$ in zone 5. Likewise, the lowest value of the ξ-coordinate of zone 5 is updated by directly injecting solution values from the $\xi = \xi_{max} - 2$ surface of zone 4. This direct injection of solution values between adjacent grid zones is a special case of a more general interpolation procedure that could be employed if the zones did not match point-for-point at the zonal interfaces.

The proper implementation of no-slip boundary conditions on the solid surfaces is dependent on the frame of reference employed. For the case of the rotating coordinate system, the impeller and shaft surfaces are assigned a zero velocity and the stationary surfaces (tank wall and side-wall baffles) are assigned a purely tangential velocity with magnitude equal to $-\omega\sqrt{x^2 + y^2}$. This no-slip boundary condition was also applied to the tank bottom (low ζ face of zone 2 and zones 4–6). The top of the tank contains a free surface that is approximated by applying z-symmetry plane boundary conditions on the high ζ face of zones 3–6.

For the general rotating flow in a mixing tank, the liquid level will be a function of radial location. However, in the limit of low rotational speed (laminar flow), the free surface is assumed to be flat and the liquid level is constant throughout the tank. Thus, neglecting the effect of surface tension, a z-symmetry boundary condition at the upper surface should be sufficient to model the laminar tank. This flat liquid level condition was verified by observation of the experimental setup discussed in the next section.

Experimental Procedure

This section describes the experimental procedure used to measure the velocity field inside the mixing tank illustrated in Figure 1. The internal tank diameter, $\tilde{D}$, was equal to the tank height, $\tilde{T}$, of 14.5 cm. A 5.08-cm-dia. pitched-blade impeller was used and was located at half the distance from the bottom of the tank to the liquid level height with a clearance, $\tilde{h}$, of 6.7 cm. This made the impeller diameter to tank diameter ratio to be 0.35, and the impeller clearance to tank diameter ratio to be 0.46. Four baffles were placed at 90° apart, and the width of each was 1.25 cm, or one-twelfth of the tank diameter.

The cylindrical tank was placed inside a square tank that was filled with the same fluid. This is done to provide a constant refraction of the laser beams across the whole tank by having a constant fluid depth. This way, the exact location of the measurement volume of the laser beams is known. A Lightnin Labmaster mixer (model TSR 1516) was used for all experiments. Silicone oil with viscosity, $\tilde{\mu} = 211$ cP, and density, $\tilde{\rho} = 1{,}049$ kg/m^3 was used as the model fluid. At an impeller rotation speed, $\tilde{N} = 100$ rpm; the Reynolds number, Re, of the stirred tank is 21, which corresponds to a laminar flow regime.

Time-averaged velocity components were measured using an LDV system, which is shown in Figure 5. The main components are a dual-channel, 2-W argon ion laser system from TSI, Inc.; a traverse controller and mechanism, which is controlled by a personal computer and is utilized to move the laser probe in a predetermined grid, and a signal processor from Aerometrics. Aerometrics also provided the software for

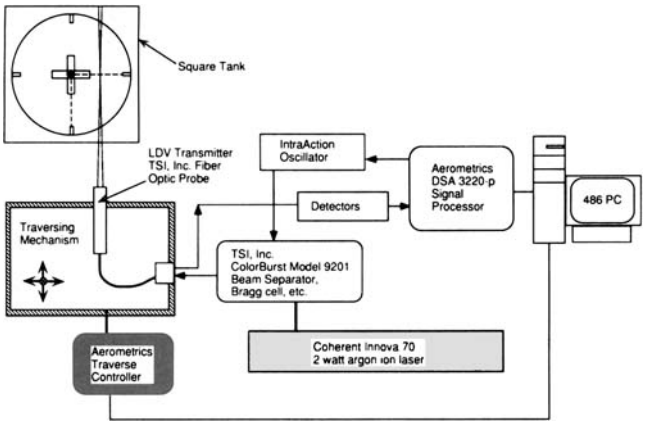

Figure 5. Experimental setup for velocity measurements.

data-acquisition and processing functions on a personal computer.

In this work, only one channel of the LDV was used to get a single velocity component at a time. The other two velocity components were obtained by readjusting the laser beams, so that all three velocity components obtained would correspond to the same relative position within the tank. Data for different velocity components were taken at two vertical (axial–radial) planes in line with the baffles to get all three components. In Figure 5, the two dashed lines drawn inside the tank represent these two planes. An almost uniformly spaced (5 mm × 5 mm) grid was set up to map out the velocity distribution of the tank. In the region around the boundary of the impeller, data were collected in a denser grid (2 mm spacing). Because of symmetry at the shaft, only one half of the tank was mapped. The seed particles were metallic coated and spherically shaped with a density of 2.6 g/cm^3 and an average diameter of 12 μm. In a typical velocity measurement using back scattering mode, a criterion of 3,600 validated points or 6-min time period was set as the end of data acquisition. Most of the velocity data had around 3,000 validated points. However, for certain small regions of the tank where the velocities were close to zero, the number of validated points was less than 100 within the 6-min time frame. The validated data were then processed and an average velocity was calculated. The resulting time-averaged velocity is presented in the next section with the computational results.

Selected data points were measured again to check for reproducibility. Up to 7,200 validated points or 12-min time frame was also set as a new criterion for the end of data acquisition. For both repeated runs using the old criterion and using this new criterion, the averaged velocities differed by less than 5% from the original data. However, when the velocities were very close to zero, variations were much greater due to insufficient validated points.

Computed Results and Discussion

In this section, the computed velocity field produced by the impeller rotating in the tank are presented. The conditions are chosen to match those in the experimental setup described in the previous section. The rotational speed of $\tilde{N} =$ 100 rpm corresponds to $\tilde{\omega} = 10.472$ rad/s. The grid is nondimensionalized by the impeller radius, $\tilde{x}_{\text{ref}} = \tilde{r}_b = 0.0254$ m and the velocity is normalized by the impeller speed, $\tilde{u}_{\text{ref}} = \tilde{\omega}\tilde{r}_b =$ 0.266 m/s.

These conditions correspond to an impeller tip speed of $\tilde{V}_t = 0.266$ m/s and an impeller Reynolds number based on tip speed and impeller radius of $Re_t = 33.59 = \pi/2\ Re$. This is in the laminar flow regime. In mixing tank literature, the Reynolds number, *Re*, is commonly reported based on rotational velocity in *revolutions* per second and impeller *diameter*, $\tilde{D}$, instead of impeller radius, $\tilde{r}_b$. However, it is more convenient in the present article, due to the nondimensionalization presented in an earlier section, to use the impeller tip Reynolds number based on impeller *radius* and rotational speed in *radians*/second.

The pseudocompressibility parameter β was set to 100 for both coarse-grid solutions and β was set to 1,000 for the fine-grid solution. For all computations the pseudotime-step $\Delta\tau$ was set to 10^{12}, which yielded the most rapid rate of convergence. Each zone of the grid was swept four times in each of the three coordinate directions at each pseudotime-step using the line relaxation algorithm. Zonal interfaces were updated implicitly at the start of each sweep.

In the experiments, the velocity was sampled over many revolutions at each point in the tank and then averaged to obtain a time-averaged θ-plane of velocity data. The sampling time was very small in comparison to the time required for one revolution of the impeller so that this averaged θ-plane represents a mean velocity field over all possible positions of the impeller relative to the side-wall baffles.

To compare the present numerical results with experiment, a spatial averaging procedure was employed. The computed velocity field was interpolated to a uniform 25×50 mesh at 30 equally spaced constant θ-planes in the flow domain. These planes were then averaged, resulting in the single, spatially averaged θ-plane of velocity data plotted in the left half of Figure 6. These results are nondimensionalized by $\tilde{u}_{\text{ref}}$ and $\tilde{x}_{\text{ref}}$ and are compared with the time-averaged velocity field measured experimentally (right half of Figure 6). The rotating impeller causes the fluid to flow radially outward, like a

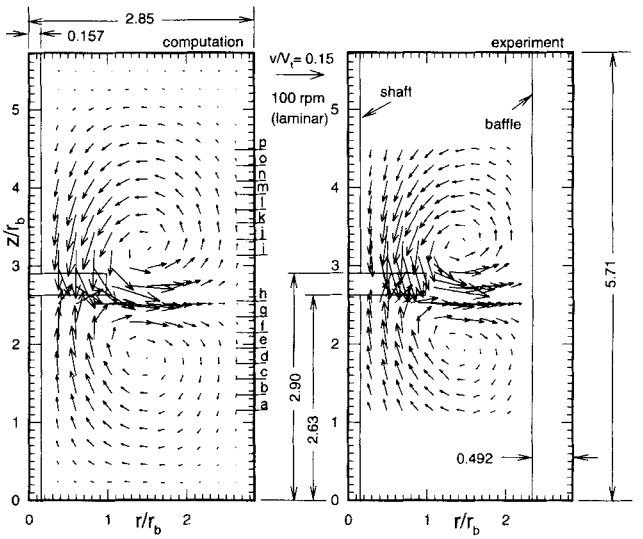

Figure 6. Comparison of velocity fields, right-half; experiment, left-half; computed (medium grid solution).

jet directed at the tank wall. Upon impinging on the outer tank wall the fluid is forced to circulate back radially inward toward the base of the impeller. This flow pattern is evident by the familiar circulating patterns both above and below the impeller. At low Reynolds numbers, the pitched blade impeller is purely a radial pumping device. As the Reynolds number is increased, the resulting direction of induced flow becomes more axial.

The experimental data were taken at the 16 axial stations labeled $a-p$ in the left half of Figure 6. The computational results and experimental results appear identical, as presented in Figure 6. Thus, a more rigorous comparison of the data is needed and the computed results are interpolated to the locations in the flow where the experimental data were taken.

Figure 7 compares computed radial and axial velocity pro-

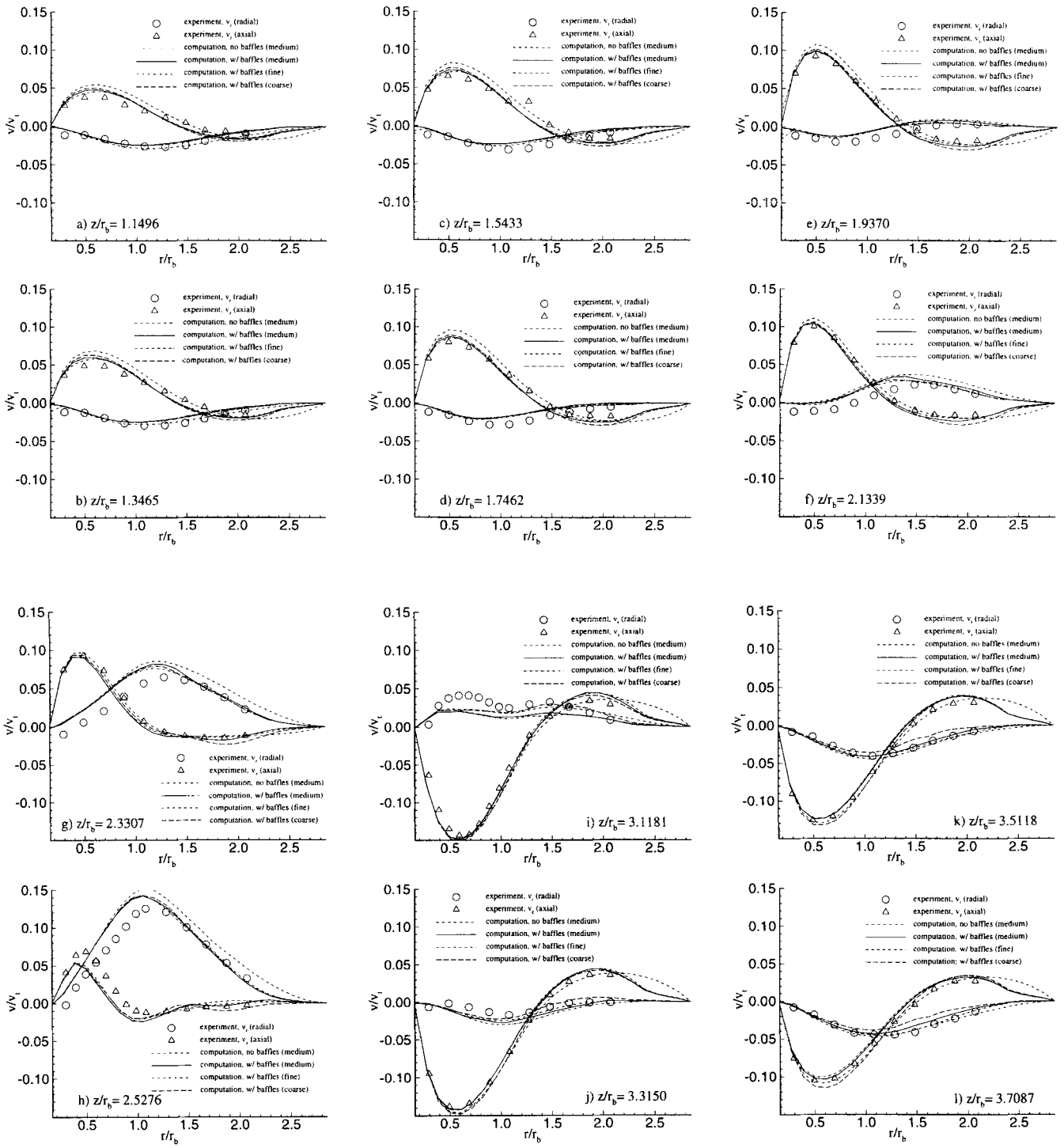

Figures 7a–7l. Comparison of axial and radial velocity profiles, stations *a–l* of Figure 6.

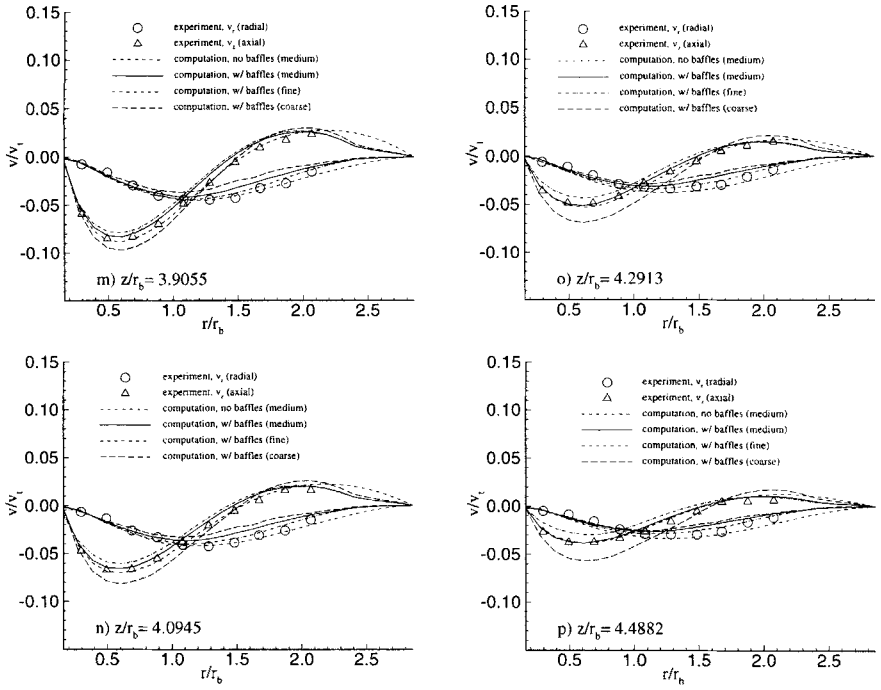

Figures 7m–7p. Comparison of axial and radial velocity profiles, stations *m–p* of Figure 6.

files with experimental data at locations *a–p* of Figure 6. Computations were performed both with and without the presence of the baffle on the medium grid and with baffles on both the coarse and fine grids. Comparison between the experimental data and the numerical predictions is quite good. Agreement is better farther away from the impeller. Directly underneath the impeller at stations *g* and *h*, the radial velocity component is overpredicted. At station *h* the axial velocity component is slightly underpredicted. Also, directly above the impeller at station *i*, the radial velocity is underpredicted. The reason for this disagreement could possibly be due to the manner in which the impeller blades were modeled. The computational grid defines impeller blades with very sharp edges, quite different from the rounded edges of the blades on the impeller used in the experimental procedure.

Overall, the axial velocity component is fairly well predicted with very small differences shown in the solution due to the presence of the baffle. The unbaffled case does predict higher radial velocities near the discharge of the impeller, which suggests a stronger recirculation exists for the unbaffled tank. As expected, both velocity components damp out more quickly toward the tank wall for the baffled tank numerical results.

The fine, medium and coarse grid solutions agree fairly well, illustrating grid independence of the numerical scheme. Computed axial velocities near the surface for the fine grid case (stations *o* and *p*) are slightly higher than experimental measurements. While the cause of this discrepancy is uncertain, quite possibly the residual of the fine-grid solution had not been reduced as much as the residual of the coarse-grid solution near the liquid surface.

Figure 8 compares tangential velocity profiles at axial stations *a–p* of Figure 6. The computations, although they qualitatively show similar trends, overpredict the tangential velocity at all stations. As expected, the computations with side-wall baffles compare better with the experiments, more so above the impeller than below the impeller. At station *i*, directly above the impeller, agreement between the baffled case and experiment is quite good. Directly below the impeller, however, at station *h*, both computations overpredict the experiments by about 25%. The cause of this error is not fully understood. The fine-grid solution, in general, agrees better with experiment than both coarser-grid numerical results. Notice that a more dramatic improvement in agreement between numerical and experimental values of the tangential velocity is observed as the grid is increasingly refined. More so than that observed for the radial and axial velocity components. The tangential velocity magnitude is not well predicted by the two coarser grids. It appears that accurate prediction of the tangential velocity requires an extremely fine grid.

Above the impeller, the tangential velocities fall off more quickly in the radial direction for the fine-grid solution with baffles. This behavior is more consistent with the experimentally measured behavior of the tangential velocity near the liquid surface. The experiments show a rather flat tangential velocity component near the surface that tends to fall off suddenly (stations *n–p*). The radial location of this abrupt fall in the magnitude of the tangential velocity decreases nearer the liquid surface. These trends are not predicted by the numerical computations, probably due to the *z*-symmetry boundary condition that is used to model the liquid surface.

Figure 9 plots the convergence history for the baffled tank computations. Approximately 450 iterations were performed for each of the three cases. At each iteration in the computations a total of four line-relaxation sweeps in each coordinate direction of *each* grid zone were performed. Note that, as the

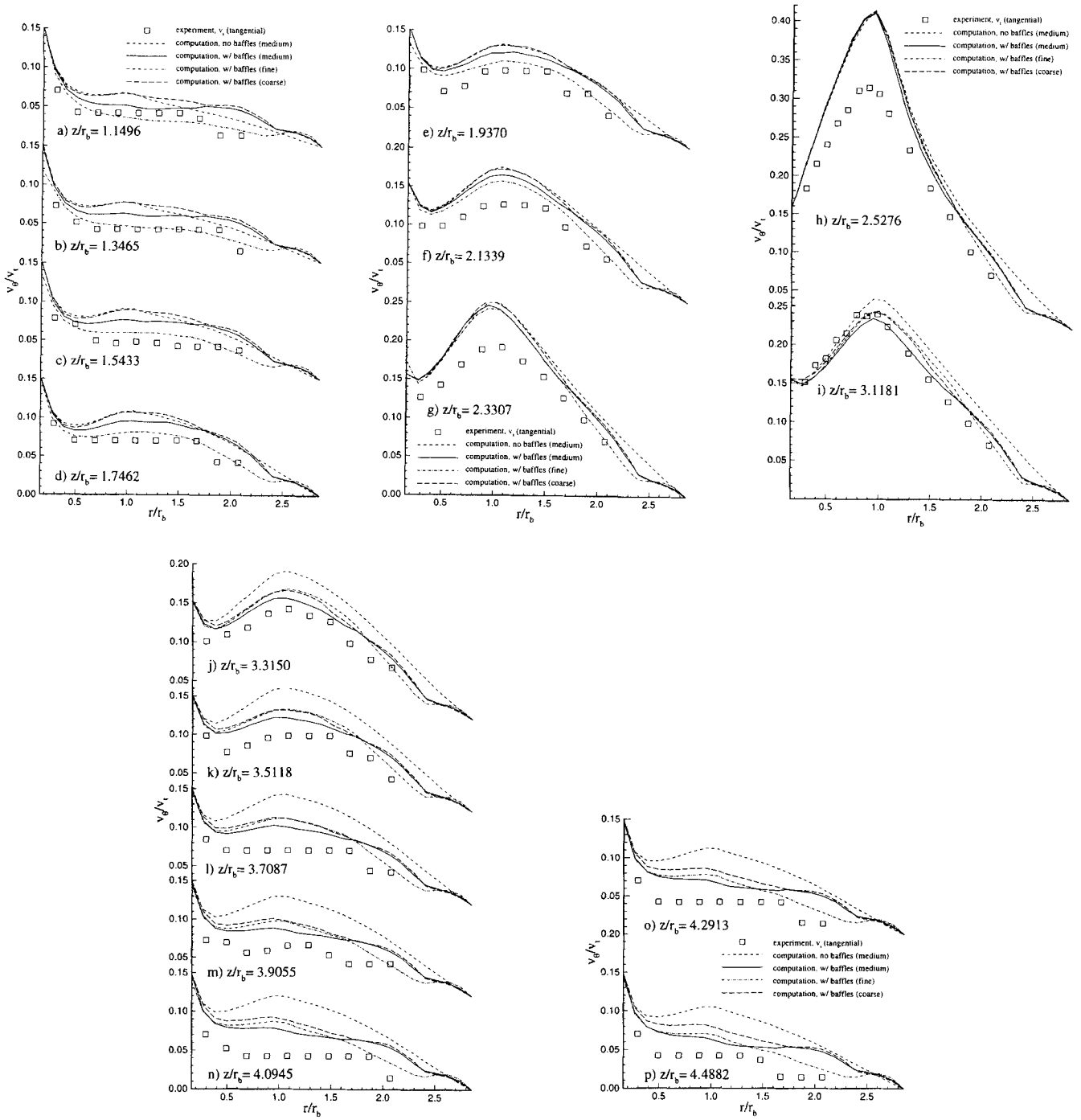

Figure 8. Comparison of tangential velocity profiles, stations *a*–*p* of Figure 6.

grid is made finer, more iterations are required to reduce the residual to a specified level using the line relaxation algorithm. CPU requirements for the baffled tank computations performed on the medium grid are summarized in Table 4. Total workstation memory requirements were approximately 40 megabytes (9.9 Mwords) of a 96-megabyte machine.

Concluding Remarks

The flow-field induced by a rotating pitched-blade impeller in a baffled mixing tank is computed using a multiblock incompressible Navier–Stokes solver. An approximate steady-state solution procedure was used that involved solving the problem from a rotating frame of reference at one position of the impeller relative to the side-wall baffles. Results of this steady-state approximation were spatially averaged and compared with time averaged experimental velocity profiles that were measured using LDV. The comparison between numerical and experimental results is shown to be quite good at low Reynolds numbers, Re = 21.

The inherent unsteady nature of the baffled, impeller-stirred tank warrants full unsteady, three-dimensional

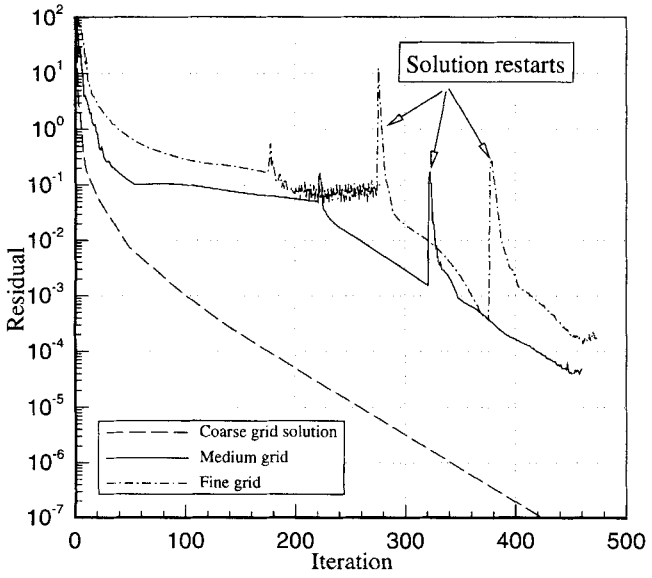

Figure 9. Convergence history for baffled tank computations.

Navier–Stokes calculations that can be quite expensive. It is shown in this article that, for relatively low Reynolds numbers, reasonably accurate axial and radial velocity component predictions can be made using the approximate steady-state method. This is expected to result in significant computational savings over full unsteady simulations.

Numerical predictions of the magnitude of tangential velocity component differ from experimental measurement by as much as 25% near the impeller. The source of this discrepancy is currently under investigation and can possibly be attributed to the symmetry boundary condition employed to model the free surface. In general, it has been found that a relatively fine mesh is needed to accurately predict the tangential velocity magnitude.

At higher Reynolds numbers the present steady-state numerical method will yield less accurate results. To accurately predict higher Reynolds number flows in stirred tanks, the turbulence must be modeled. Work illustrating how numerical predictions of velocity using the present steady-state method compare with experiment as a function of increasing Reynolds number is the subject of a future study.

Acknowledgments

The authors would like to thank Doug Leng, David West, Hank Kohlbrand, and John Serratelli of The Dow Chemical Company for their continued support of this research. Also thanks goes to Scott Reynolds for his work with the LDV experiments performed in the Dow Chemical Company Central Research Mixing Laboratory.

Table 4. Computational Requirements

Machine	CPU (s)	CPU (s/Iter.)	CPU (s/Iter./Group)
SGI R4000 Indigo	403,652	897	40.2×10^{-4}
Cray C90	14,049	31	1.4×10^{-4}

Notation

$\tilde{a}, a$ = tilde denotes dimensional quantities; quantities without a tilde are made dimensionless using $\tilde{u}_{\text{ref}}$ and/or $\tilde{x}_{\text{ref}}$, unless explicitly stated otherwise
$\tilde{d}$ = impeller diameter
p = thermodynamic pressure
$\underline{Q}$ = vector of dependent variables
$\tilde{r}$ = radial distance from tank centerline
t = time
U = contravariant velocities
u, v, w = Cartesian velocity components
$\tilde{V}_t$ = impeller tip speed, $\tilde{\omega}\tilde{r}_b$
x, y, z = Cartesian coordinate directions
$\tilde{\nu}$ = kinematic viscosity, $\tilde{\mu}/\tilde{\rho}$
$\omega_x, \omega_y, \omega_z$ = Cartesian components of the rotational vector with magnitude Ω, (rad/s)

Literature Cited

Anderson, D. A., J. C. Tannehill, and R. H. Pletcher, *Computational Fluid Mechanics and Heat Transfer*, Hemisphere (1984).

Gosman, A. D., J. Y. Luo, and R. I. Issa, "Full Flow Field Computation of Mixing in Baffled Stirred Tanks," Paper No. 109c, AIChE Meeting, Miami Beach, FL (1992).

Hoffmann, K. A., *Computational Fluid Dynamics for Engineers*, Engineering Education System, Austin, TX (1989).

Hiraoka, S., I. Yamada, T. Aragaki, H. Nishiki, A. Sata, and T. Takagi, "Numerical Analysis of Three-Dimensional Velocity Profile of Highly Viscous Newtonian Fluid in an Agitated Vessel with Paddle Impeller," *J. Chem. Eng. Japan*, **21**, 79 (1988).

Kaminoyama, M., and M. Kamiwano, "Numerical Analysis on Power Consumption and Mixing Time of a Highly Viscous Pseudoplastic Liquid in Geometrically Similar Paddle Impeller Mixers," in *Proc. 7th European Conf. on Mixing*, Brugge, Belgium, p. 545 (1991).

Kiris, C., J. L. Chang, D. Kwak, and S. E. Rogers, "Incompressible Navier-Stokes Computations of Rotating Flows," AIAA Paper 93-0678, Reno, NV (Jan., 1993).

Preng, C.-Y., and J. Y. Murthy, "A Moving Mesh Technique for the Simulation of Flow in Mixing Tanks," Paper No. 109b, AIChE Meeting, Miami Beach, FL (1992).

Rogers, S. E., D. Kwak, and C. Kiris, "Steady and Unsteady Solutions of the Incompressible Navier-Stokes Equations," *AIAA J.*, **29**, (Apr., 1991).

Rogers, S. E., and D. Kwak, "Upwind Differencing Scheme for the Time-Accurate Incompressible Navier-Stokes Equations," *AIAA J.*, **28** (Feb.,1990).

Rogers, S. E., D. Kwak, and U. Kaul, "On the Accuracy of the Pseudocompressibility Method in Solving the Incompressible Navier-Stokes Equations," *Appl. Math. Modelling*, **11** (Feb., 1987).

Manuscript received Sept. 29, 1994, and revision received Dec. 9, 1994.